A comparison of weight average and direct boundary fitting of sedimentation velocity data for indefinite polymerizing systems

C.A. Sontag[a], W.F. Stafford[b], J.J. Correia[a],*

[a]*Department of Biochemistry, University of Mississippi Medical Center, 2500 North State Street, Jackson, MS 39216, USA*
[b]*Analytical Ultracentrifugation Research Laboratory, Boston Biomedical Research Institute, Watertown, MA 02472, USA*

Abstract

Analysis of sedimentation velocity data for indefinite self-associating systems is often achieved by fitting of weight average sedimentation coefficients ($\hat{s}_{20,w}$). However, this method discriminates poorly between alternative models of association and is biased by the presence of inactive monomers and irreversible aggregates. Therefore, a more robust method for extracting the binding constants for indefinite self-associating systems has been developed. This approach utilizes a set of fitting routines (SedAnal) that perform global non-linear least squares fits of up to 10 sedimentation velocity experiments, corresponding to different loading concentrations, by a combination of finite element simulations and a fitting algorithm that uses a simplex convergence routine to search parameter space. Indefinite self-association is analyzed with the software program ISODESfitter, which incorporates user provided functions for sedimentation coefficients as a function of the degree of polymerization for spherical, linear and helical polymer models. The computer program HYDRO was used to generate the sedimentation coefficient values for the linear and helical polymer assembly mechanisms. Since this curve fitting method directly fits the shape of the sedimenting boundary, it is in principle very sensitive to alternative models and the presence of species not participating in the reaction. This approach is compared with traditional fitting of weight average data and applied to the initial stages of Mg^{2+}-induced tubulin self-associating into small curved polymers, and vinblastine-induced tubulin spiral formation. The appropriate use and limitations of the methods are discussed.
© 2003 Elsevier B.V. All rights reserved.

Keywords: Sedimentation velocity; Polymerizing systems; Frictional coefficient

1. Introduction

Analytical ultracentrifugation is a powerful method for investigating the association properties of macromolecular complexes. Numerous applications have been reported dating back to the original work by Svedberg on hemoglobin [1]. Many biochemical systems exhibit complex reaction path-ways or broad size distributions that make them best analyzed by sedimentation velocity approaches [2]. One of the traditional methods for analyzing sedimentation velocity data for interacting systems is by analysis of the concentration dependence of the weight average sedimentation coefficient ($\hat{s}_{20,w}$). For example, numerous ultracentrifuge studies have been performed on the ligand-induced self-association of tubulin, the major protein found in microtubules [2]. These ligands include Mg^{2+} [3,4], drugs like vinca alkaloids [5–10], and microtubule associated proteins like MAP2 [11]

*Corresponding author. Tel.: +1-601-984-1522; fax: +1-601-984-1501.
E-mail address:
jcorreia@biochem.umsmed.edu (J.J. Correia).

and stathmin [12,13]. The $\hat{s}_{20,w}$ analysis is based upon the thermodynamic requirement that the weight average sedimentation coefficient of a system is determined by mass action, and will be a unique function of the composition of the solution at the plateau concentration. Weight average analysis techniques are highly appropriate for determination of the stoichiometry and thermodynamics of the interactions. This approach is complex because two parameters must be specified for each oligomer in the reaction, the molecular weight M_i and the frictional coefficient f_i, to be able to assign the appropriate sedimentation coefficient S_i. In sedimentation equilibrium analysis the number of parameters is reduced to one per species, the molecular weight M_i. However, many reaction schemes span an extremely broad range of molecular weights, and thus it is difficult to choose a rotor speed where all of the species are contributing to the equilibrium distribution analyzed, i.e. the largest species pellet out of solution. The advantage of velocity analysis is the entire boundary, and thus the entire reactive species distribution, is measured and contributes to the average $\hat{s}_{20,w}$ behavior and to the overall shape of the boundary.

Significant progress has been made in simulating the shapes of sedimenting boundaries for various noninteracting and interacting systems [14–22]. These include nonideal, discrete reaction mechanisms like monomer–dimer, monomer–trimer, monomer–dimer–tetramer–octomer, isodesmic or indefinite association [23], and heterogeneous systems like $A + B \leftrightarrow C$, $C + B \leftrightarrow D$ [21,24]. A major goal of these efforts is to take advantage of modern computing power and incorporate these simulation methods into non-linear least squares (NLLS) fitting algorithms that directly compare experimental data with distinct reaction mechanisms. When done in a global context, these approaches offer highly robust methods for determining stoichiometry and the equilibrium constants for the interactions. Direct inspection of the deviations and RMS of the fits allows statistically significant discrimination between models and discovery of nonequilibrium complications, such as inactive monomers or the presence of irreversible aggregates.

Particularly challenging problems for sedimentation velocity analysis are proteins that undergo indefinite or isodesmic self-association schemes. Examples include tubulin [3,5,10], insulin self-association in the absence of Zn^{+2} [25], spectrin [26], glutamate dehydrogenase [27], myelin basic protein in the presence of detergents [28], FtsZ [29,30], and Rev [31,54]. In this study, we report the development of a fitting routine (ISODESfitter) that globally analyzes up to 10 sedimentation velocity data sets collected as a function of loading concentration for the equilibrium constant for indefinite self-association. ISODESfitter uses a combination of finite element simulations of the reaction boundary [32,33] and a NLLS fitting algorithm that involves a simplex convergence routine to search parameter space to fit to time difference, ΔC, data [34]. The form of the $S(N)$ vs. N-mer function is generated by simulations with HYDRO [35] to generate the data for different models corresponding to constant axial ratio ($N^{2/3}$), linear polymers and helical or curved polymers. These models were incorporated into both $\hat{s}_{20,w}$ and ΔC fitting functions which in turn have been applied to data from the early stages of Mg^{2+}-induced self-association of tubulin and vinblastine-induced tubulin spiral formation.

2. Methods

2.1. Tubulin purification

MAP-free pig brain tubulin was obtained by two cycles of warm–cold polymerization–depolymerization followed by phosphocellulose chromatography (PC) to separate tubulin from MAPs [36,37]. Protein concentrations were determined spectrophotometrically, $\varepsilon_{278} = 1.2 \, l \, g^{-1} \, cm^{-1}$ [38]. An additional tubulin recycling step was performed in order to further remove any denatured tubulin. This involved diluting tubulin 1:1 with 8 M glycerol, 0.1 M Pipes, 1 mM $MgSO_4$, 1 mM EGTA and bringing the final concentration of GTP and $MgSO_4$ to 0.5 and 2.5 mM, respectively. The samples were incubated at 37 °C for 30 min and then spun at 100 000 rpm in a TL-100 ultracentrifuge (TLA 100.1) for 5 min at 37 °C. The pellets were resuspended by douncing 10 times in a

minimum volume of a buffer consisting of 100 mM Pipes, 1 mM MgSO$_4$, 2 mM EGTA, 2 mM DTT, 0.5 mM GDP, pH 6.9. The resuspended tubulin was clarified by spinning at 100 000 rpm (rotor TLA 100.3) for 3 min at 4 °C. Finally, the recovered tubulin supernatant was frozen dropwise into liquid N$_2$ and stored at −70 °C.

2.2. Sedimentation velocity experiments

Sedimentation studies were performed in a Beckman Optima XLA analytical ultracentrifuge equipped with absorbance optics and an An60 Ti rotor. Velocity data were collected at the appropriate speeds at a wavelength of 278 nm using a spacing of 0.002 cm with one flash at each point in continuous scan mode. Tubulin self-association was examined by spinning tubulin from 2 to 14 μM over a range of MgCl$_2$ concentrations, 0–10 mM, at 3.6 °C, 42 000 rpm in a buffer consisting of 25 mM Pipes, 50 mM KCl, 50 μM GDP, 1 mM EGTA, pH 6.8, titrated with KOH (buffer P). Runs were conducted at 3.6 °C to minimize irreversible tubulin aggregation. Temperature was calibrated by the method of Liu and Stafford [39]. Samples were equilibrated in buffer P by centrifugal gel filtration with Sephadex G-50 columns [40].

2.3. Sedimenting boundary analysis

All sedimentation velocity data were initially analyzed by DCDT+ (version 1.15) [16,22] as described [41] to produce $g(s)$ distribution plots. The weight average sedimentation coefficient values ($\hat{s}_{20,w}$) were obtained from DCDT+ corrected for the solution density and viscosity [42]. The density for each buffer was measured using an Anton Paar DMA 5000 density meter and the viscosities were measured in a Cannon-Manning Semi-Micro viscometer placed in a Cannon M1 Series constant temperature water bath. The measured densities at 3.6 °C for 0, 0.5, 1, 2, 5, and 10 mM Mg^{2+} buffers were 1.006878, 1.006905, 1.006935, 1.006835, 1.007015, and 1.007122 g ml^{-1}, respectively. The viscosities were measured at 24.7 °C and these values were corrected to 3.6 °C. The converted viscosities at 3.6 °C were

1.5996, 1.5980, 1.6013, 1.6609, 1.6631 and 1.6686 cP, respectively. The partial specific volume used for tubulin was 0.736 ml g^{-1} [43,44].

2.4. $\hat{s}_{20,w}$ Analysis of tubulin self-association

Fitting of $\hat{s}_{20,w}$ data was accomplished through the use of a nonlinear least-squares program FITALL (MTR Software, Toronto, Canada) that had been modified to include various fitting functions to obtain the appropriate binding constants involved [2]. This approach requires an estimate of S_1 the tubulin-heterodimer sedimentation coefficient and estimates of the S_i values for each polymer species participating in the isodesmic reaction. (An isodesmic reaction implies equal association constants, K_{iso}, for each step in the assembly pathway, as discussed below.) S_1 was estimated by linear extrapolating of $\hat{s}_{20,w}$ values to zero Tb concentration. The extrapolated sedimentation coefficient values at 0, 0.5, and 1 mM Mg^{2+} converged to a value of 5.82 ± 0.05 S$_{20,w}$, consistent with previous reports [3,4], and was used for all data sets. The S_i values were generated from an $N^{2/3}$ model, a linear model or a helical self-association model (Section 2.6). $\hat{s}_{20,w}$ analysis also allows for the inclusion of hydrodynamic nonideality in the form $S \times (1 - gC)$, where g has been measured to be 0.018 ml mg^{-1} [3,4] and C is the total protein concentration. If we assume $g = 0.0$, then K_{iso} is between 26.7 (at 0 mM Mg^{2+}) and 7.6% (at 10 mM Mg^{2+}) smaller, corresponding to a decrease in ΔG_{iso} of 0.13–0.04 kcal mol^{-1}.

2.5. Direct curve fitting analysis of the sedimenting boundary

A curve fitting procedure has been developed using both least squares and robust statistical methods for the determination of equilibrium constants for interacting systems from sedimentation velocity experiments [24,55]. Time differences of the concentration profiles are employed to achieve automatic removal of time-independent baseline components from the raw data. Curve fitting is carried out using a simplex directed search [34] and employing the finite element method of Claverie [32,33] to solve the Lamm equation for each

Table 1
Summary of HYDRO derived functions for fitting $\text{Ln}(S_N)$ vs. $\text{Ln}(N)$

$N^{2/3}$	$\ln(s/s_1) = (2/3)(\ln(j))$
Linear (spheres)	$\ln(s/s_1) = 0.4388(\ln(j)) - 0.03172(\ln(j))^2$
Linear (21 beads)	$\ln(s/s_1) = 0.5932(\ln(j)) - 0.05360(\ln(j))^2$
Helical (spheres)	$\ln(s/s_1) = 0.3664(\ln(j)) - 0.01102(\ln(j))^2$
Helical (21 beads)	$\ln(s/s_1) = 0.4911(\ln(j)) - 0.0006354(\ln(j))^2$
Helical (42 beads)	$\ln(s/s_1) = 0.4315(\ln(j)) - 0.01306(\ln(j))^2$

set of new estimates generated by the Nelder and Mead algorithm. Solutions are generated for the times corresponding to the experimental traces and are subtracted pairwise to generate simulated time difference ΔC patterns. All S_1 and S_i values correspond to the solution conditions and the temperature of the experiment. The experimental and simulated time difference patterns are compared and further estimates generated until either the sum of the squares of the residuals or the sum of the absolute values of the residuals is minimized. The finite element method was adapted to solve various isodesmic self-associating models, characterized by the equilibrium constant K_{iso}. This allows us to quantify the extent of Mg^{2+}- and vinblastine-dependent tubulin self-association into small curved and helical polymers. The isodesmic fitter, ISODESfitter, allows one to input a quadratic or cubic relationship between the logarithm of the sedimentation coefficients of the oligomeric species (S_n/S_1) present and the logarithm of their corresponding degree of oligomerization or N-mer value (Table 1). The models tested were constant axial ratios $(S_i = (i)^{2/3}S_1)$, linear, or helical polymers. These models also allow for the inclusion of hydrodynamic nonideality, g, and thermodynamic nonideality, BM1 [55]. In general, inclusion of a fixed value of $g = 0.018$ ml mg^{-1} has a small effect on RMS ranging from ± 0.002 with no consistent improvement in the fitting. K_{iso} values are slightly increased as expected.

2.6. HYDRO modeling

Hydrodynamic models for tubulin polymers were simulated with HYDRO (Hydro5amsd.exe; [35]) in two ways. Either each tubulin subunit was modeled as a single sphere of fixed radius (30.07 Å) or the tubulin dimer was modeled as 42 beads of 13 Å radius (21 beads for each subunit; provided by Diaz and Andreu) derived from scattering data [45,46]. These values along with a vbar of 0.736 ml g^{-1} gave a heterodimer sedimentation coefficient of 5.82 $S_{20,w}$. The sphere and dimer models were then allowed to propagate into either a linear polymer or a helical polymer using a contacted step size of 4–8 nm. The helix dimensions correspond to a pitch of 25.67 nm and a diameter of 38.35 nm as described for vinblastine induced polymers by Hodgkinson et al. [47]. Data were simulated at intervals of 5–10 dimers for up to 50 dimers, plotted as $\text{Ln}(S_N/S_1)$ vs. $\text{Ln}(N)$ and fit as a quadratic function in $\text{Ln}(N)$ (Table 1). (For cases where S_N was simulated up to 100- to 300-mers we used cubic functions.) For the sphere model each sphere was centered on the helical arc, while for the 42-bead model each dimer unit was rigidly translated in a 8 nm helical step. This assumes bending occurs only at the hetero-dimer interface. A 21-bead model was also constructed where each monomer unit was rigidly translated in a 4 nm helical step. This assumes bending occurs at each subunit interface. Simulations with a 21-bead model give identical results to the 42-bead model for the linear case and nearly identical results for the helical case (Fig. 1). These quadratic (or cubic) functions are then used as the $S(N)$ vs. N data generators in the weight average and ISODES fitters (Fig. 3). For small degrees of association these helical polymers approximate the quaternary structures of small curved polymers. Other models are possible but no data exist to limit the choices (Section 4).

3. Results

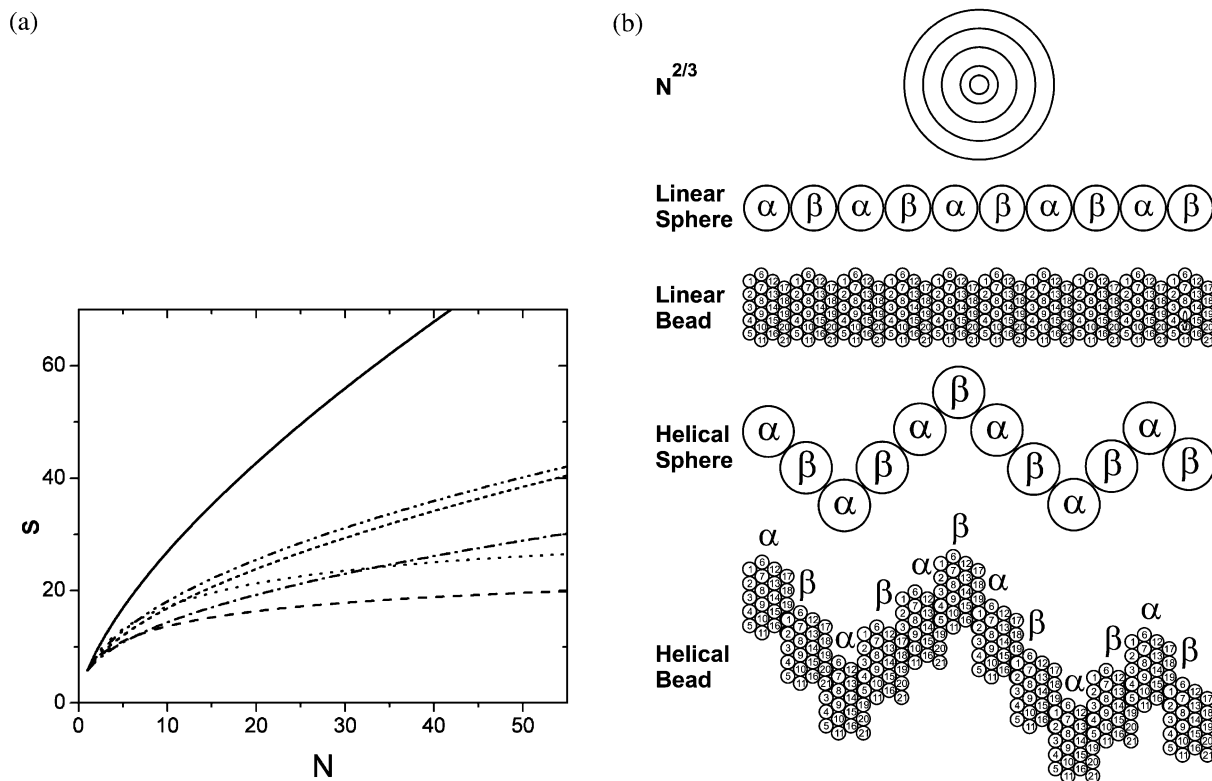Fig. 1A summarizes the dependence of s on the degree of oligomerization simulated with HYDRO

(a)

(b)

Fig. 1. (A) Models for calculating $S(N)$ vs. N-mer corresponding to $N^{2/3}$(——), linear using spheres (– – –), linear using 21-bead model (····), helical using spheres (-··-··-), and helical using 21-bead model (-···-···-) or 42-bead model (- - - -) polymer structures. The linear and helical models were constructed using HYDRO generated data. The linear spherical data is consistent with either a Perrin rod or prolate model of similar axial ratios (not shown; [53]). S_1 equals 5.82 s in all cases, the experimental $S_{20,w}$ for tubulin dimers. (B) Graphical depictions of the various models used in Fig. 1A. The $N^{2/3}$ model assumes constant axial ratio for all polymers, represented here by spheres, but not restricted from other axial ratios. The linear models assume bead deflections along a single axis. The helical models are defined by the helical rise and pitch of vinblastine induced spirals (see Section 2). For 42-bead helices the helical bend is between dimers, while for 21-bead helices the bend is both within the dimer and between dimers.

for various polymer configurations (Fig. 1B). The $N^{2/3}$ or constant axial ratio model is, as expected, the steepest since it involves the formation of the most compact polymers possible. The linear spheres and the linear 21- or 42-bead models are relatively flat above 20-mers and asymptote to 20 and 27 S, respectively. The helical spheres and the helical 21- or 42-bead models deviate from their corresponding linear models above 8-mers and continue to have significant slope above 50-mers. These models were incorporated into weight average and direct boundary shape fitting algorithms.

To demonstrate the influence of these six models on data analysis, sedimentation coefficient distributions $g(s)$ were simulated for increasing K_{iso}

values and for different quaternary models. Fig. 2A presents the $N^{2/3}$ results for increasing K_{iso} values ranging from 5×10^4 to 5×10^6. There is a significant increase in the peak position, the weight average value and the degree of trailing or centripetal skewing with increasing indefinite association constant. In Fig. 2B different models are simulated at a fixed K_{iso} value of 5×10^6. It is dramatically apparent that even though the species distribution is the same (Fig. 2C), the $g(s)$ patterns in Fig. 2B are different because of the $S(N)$ vs. N dependency for the different models. In general, the linear and helical polymers sediment much more slowly due to increased frictional drag. Only sedimentation velocity analysis can discriminate between the
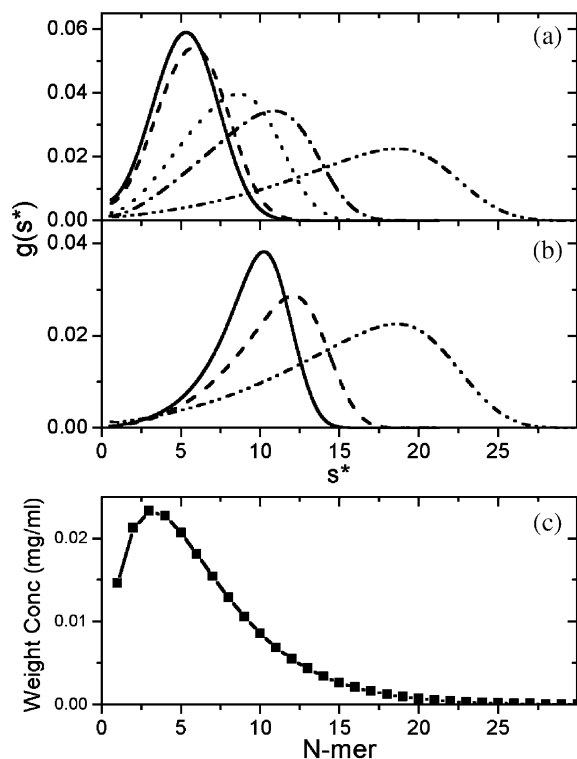
Fig. 2. Simulated $g(s)$ patterns for isodesmic tubulin data. The sedimentation scans were generated with the simulation option in ISODESfitter, and the $g(s)$ patterns were generated with DCDT+. An apparent value of S_1 (5.15 s), corresponding to the vinblastine experiments, is used to generate the $g(s)$ curves. Panel A. $g(s)$ patterns as a function of K_{iso} for 5E4, 1E5, 5E5, 1E6, 5E6 M^{-1} (left to right) were generated at a fixed tubulin concentration (2.0 μM) using the $N^{2/3}$ model for polymer S_n values. Panel B. $g(s)$ patterns at $K_{iso}=5$E6 and [Tb]$=2.0$ μM were generated for a spherical linear model (—), a 42-bead helical model (– – –) and the $N^{2/3}$ model ($\cdots\cdots$) for polymer S_n values. Panel C. A plot of the initial species distribution ([mg ml^{-1}] vs. N-mer; at time$=0$ s) generated for 2 μM tubulin at a K_{iso} of 5E6 M^{-1}.

models. These models would be identical if analyzed by equilibrium approaches because the MW and species distributions would be identical. The question is does fitting velocity data with these various models allow one to discriminate between them and thus choose the best model to describe the data?

Fig. 3 summarizes the species distribution $g(s^*)$ for data collected for PC-tubulin as a function

Mg^{2+} and protein concentration. It is apparent that the $g(s)$ patterns shift with both increasing protein and divalent cation concentration. The easiest method for quantitatively analyzing these data is to fit the $\hat{s}_{20,w}$ vs. tubulin concentration data to an appropriate association scheme [2]. Tubulin is known to undergo a Mg-dependent indefinite self-association that terminates in 42 S ring formation [3,4]. For these Mg^{2+} and protein concentrations the majority of the $\hat{s}_{20,w}$ values are less than the expected value for tubulin dimers. Thus, these data correspond to the early stages of indefinite polymerization and were fit to a K_{iso} model (Table 1) for six different $S(N)$ functions (Table 1 and Fig. 1).

Fig. 4 summarizes the fitting for $N^{2/3}$, a 21-bead linear and a 21-bead helical model. Fitting with an $N^{2/3}$ model produces reasonably good fits for all data sets. At 0, 0.5 and 1 mM Mg^{2+} the models are equally good at describing the data. At 2 and 5 mM Mg^{2+} the $N^{2/3}$ model is the worst fit. (This is exaggerated at 5 mM Mg^{2+} by the presence of two outliers, discussed below.) At 10 mM Mg^{2+} the $N^{2/3}$ model is again the best fit, primarily because it rises so steeply with N-mer and therefore can more easily follow the rapid rise of the $\hat{s}_{20,w}$ data. There is also a significant improvement of the 21–42 bead models over the two sphere models. In general K_{iso} values vary with the steepness of the $S(N)$ models, being largest with the linear and helical sphere models (Table 2). The K_{iso} values for the sphere models are on average 1.34–1.67$\times$larger relative to the 21- and 42-bead models, and 2.08–4.71$\times$larger relative to the $N^{2/3}$ model, consistent with the smaller S_i values and the need to increase K_{iso} to compensate.

A further test of this analysis is to perform Wyman analysis (Fig. 5A) of the Ln(K_{iso}) values as a function of Ln[Mg^{+2}]. Surprisingly, all of the models give slopes that are consistent with the binding of one Mg^{2+} per addition of tubulin heterodimer, 0.812 ± 0.056, as reported previously [3,4]. This suggests fitting of weight average data correctly tracks the trends in the data and Wyman analysis of these data (∂Ln K_{iso}/∂Ln[Mg^{+2}]) is remarkably forgiving of incorrect models.
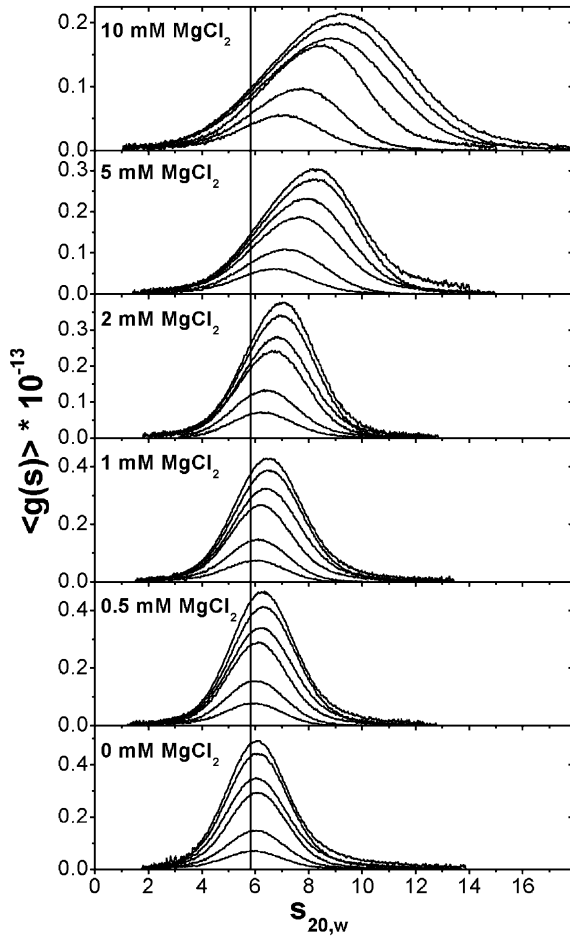
Fig. 3. A family of $g(s)$ plots demonstrating the increasing degree of tubulin self-association with increasing Mg^{2+} concentration (0–10 mM Mg^{2+}). For each Mg^{2+} concentration, sedimentation velocity runs are preformed using a range of 2–14 µM tubulin. Within each Mg^{2+} concentration there is a noticeable shift in the $g(s)$ curves, demonstrating that the degree of self-association is influenced by both an increase in Mg^{2+} and tubulin concentration. The sedimentation coefficient for the tubulin dimer S_1 is indicated by the vertical line, and determined by extrapolation of $\hat{s}_{20,w}$ data to zero protein concentration.

Fig. 6 summaries a global ISODES fit of the six 10 mM Mg^{2+} data sets from Fig. 3 to the 42-bead helical model. What is apparent in Fig. 6 is that the fits (red lines) are shifted towards lower radial positions for the two lowest concentrations (left column), while the fits track through the data

or are slightly shifted towards higher radial positions for the four highest concentrations. The global K_{iso} for these data is 2.31×10^5, a nearly identical value to that for the fitting of weight average data to a 42-bead helical model. What this analysis allows us to see on a specific sample basis is the deviations from the best fit. In this instance there appears to be heterogeneity in K_{iso}. In addition, in three of the samples at 8, 10 and 14 µM loading concentration, there is significant deviation at the base of the cell since the fits come back to baseline while the data (in black) retains a gradient. If this deviation were due to presence
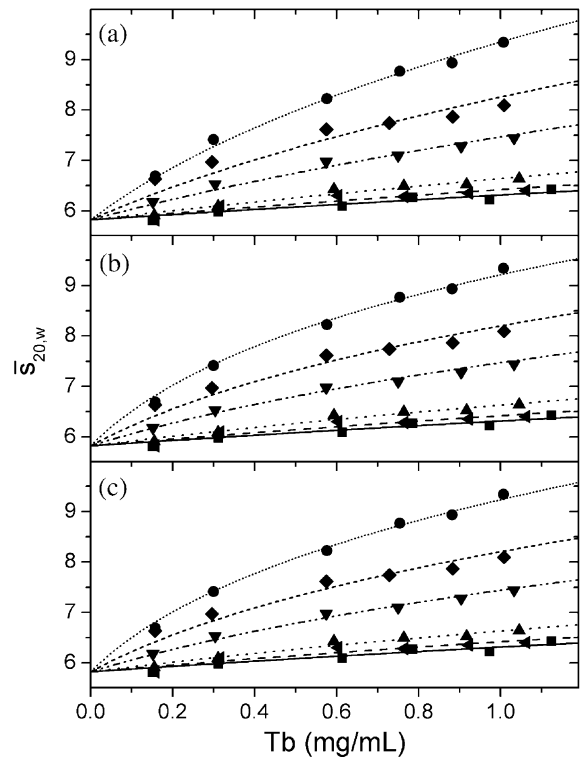

Fig. 4. A comparison of fitting $\hat{s}_{20,w}$ data using different models for Mg^{2+} induced tubulin self-association. The closed symbols (■, ◄, ▲, ▼, ♦, ●) represent the $\hat{s}_{20,w}$ values for each tubulin concentration, 2–14 µM, at each corresponding Mg^{2+} concentration: 0, 0.5, 1, 2, 5, and 10 mM, respectively. The curves represent the fits to the $\hat{s}_{20,w}$ data assuming an $N^{2/3}$ (panel A), a 21-bead linear (panel B), or 21-bead helical (panel C) relationship between the sedimentation coefficients and the polymers formed. A summary of the fits to all six models (Fig. 1) is listed in Table 2.

Table 2
Summary of $\hat{\mathbf{s}}_{20,w}$ fitting of sedimentation velocity data

		[Mg^{2+}] (mM)					
		0	0.5	1	2	5	10
$N^{2/3}$	$\sigma^2_{[fit]}$ (S)	0.00432	0.00573	0.00310	0.00580	0.0417	0.00559
	K_{iso} (M^{-1})	9.90×10^3	1.19×10^4	1.61×10^4	3.50×10^4	5.75×10^4	9.67×10^4
	$\Delta G°K_{iso}$ (kcal mol^{-1})	-5.06	-5.16	-5.33	-5.75	-6.02	-6.31
Linear (spheres)	$\sigma^2_{[fit]}$ (S)	0.00510	0.00517	0.00295	0.00138	0.00627	0.0530
	K_{iso} (M^{-1})	1.86×10^4	2.27×10^4	3.19×10^4	8.02×10^4	1.52×10^5	3.04×10^5
	$\Delta G°K_{iso}$ (kcal mol^{-1})	-5.41	-5.52	-5.70	-6.21	-6.56	-6.94
Linear (21 beads)	$\sigma^2_{[fit]}$ (S)	0.00465	0.00528	0.00288	0.00234	0.0192	0.0140
	K_{iso} (M^{-1})	1.30×10^4	1.64×10^4	2.16×10^4	5.03×10^4	8.83×10^4	1.62×10^5
	$\Delta G°K_{iso}$ (kcal mol^{-1})	-5.21	-5.34	-5.49	-5.95	-6.26	-6.60
Helical (spheres)	$\sigma^2_{[fit]}$ (S)	0.00516	0.00516	0.00300	0.00139	0.00786	0.0366
	K_{iso} (M^{-1})	2.21×10^4	2.69×10^4	3.79×10^4	9.49×10^4	1.76×10^5	3.43×10^5
	$\Delta G°K_{iso}$ (kcal mol^{-1})	-5.50	-5.61	-5.80	-6.30	-6.64	-7.01
Helical (21 beads)	$\sigma^2_{[fit]}$ (S)	0.00470	0.00539	0.00289	0.00229	0.0199	0.0109
	K_{iso} (M^{-1})	1.51×10^4	1.83×10^4	2.53×10^4	5.90×10^4	1.03×10^5	1.87×10^5
	$\Delta G°K_{iso}$ (kcal mol^{-1})	-5.29	-5.40	-5.58	-6.04	-6.35	-6.68
Helical (42 beads)	$\sigma^2_{[fit]}$ (S)	0.00484	0.00530	0.00289	0.00178	0.0158	0.0158
	K_{iso} (M^{-1})	1.75×10^4	2.13×10^4	2.96×10^4	7.04×10^4	1.25×10^5	2.31×10^5
	$\Delta G°K_{iso}$ (kcal mol^{-1})	-5.37	-5.48	-5.66	-6.14	-6.45	-6.79

These sedimentation velocity experiments were performed at 4 °C, $\lambda = 278$ nm, and 42 000 rpm using the 25 mM Pipes buffer at pH 6.8 with 50 μM GDP and 50 mM KCl. The global $\hat{\mathbf{s}}_{20,w}$ fits used a fixed sedimentation coefficient value for tubulin of 5.82 $S_{20,w}$ and $g = 1.8 \times 10^{-2}$ for all fits.

of a larger reversible polymer like a ring, then the deviation should increase in a concentration dependent manner, being most evident in the higher concentrations. The fact the 12-μM sample does not exhibit this deviation suggests that this behavior is not due to reversible ring formation. This suggests the presence of larger aggregates not participating in the reversible reaction.

Fig. 7 summarizes individual ISODES fits of the same 10 mM Mg^{2+} data with a 42-bead helical model. Unlike weight average analysis, an advantage of direct boundary fitting is that the analysis can be done on single experiments. All of the individual fits now track the low radius side of the boundaries indicating an improvement in the fits. The K_{iso} values range from 2.12 to 2.79×10^5 M^{-1}, with an average of 2.37 (± 0.22)$\times 10^5$ M^{-1}, consistent with the global value, 2.31×10^5 M^{-1}. The individual fits do not account for the

presence of larger aggregates in three of the samples, and, as with the global fits, the deviation at the base of the cell is ignored in the individual fits, which instead follow the major trends in the data. An additional possibility for analysis of this type [18] is to significantly limit the fitting range, < 6.8 cm, or to choose later scans in the analysis, to avoid this portion of the data. It is quite apparent this will have little impact on the K_{iso} values, since the fits already appear to ignore this portion of the data curves.

Table 3 summarizes the results of global fits of all data sets using all six model functions for $S(N)$. In general and similar to weight average analysis, no model is preferred in describing the data. Each $S(N)$ function reveals both the presence of heterogeneity and larger aggregates. The linear and helical sphere models give global K_{iso} values that are systematically larger than the 21- and 42-bead
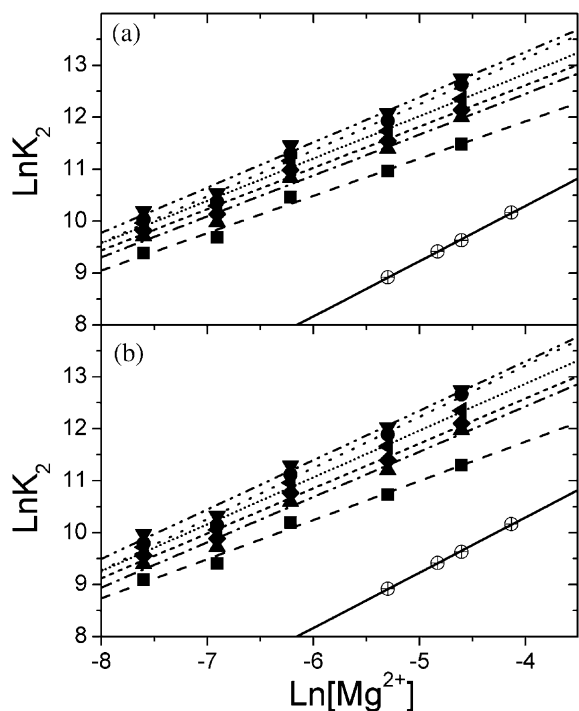
Fig. 5. A Wyman linkage plot of the binding constants obtained from fitting the Mg^{2+} induced tubulin self-associating data. The slopes of these lines correspond to the number of Mg^{2+} ions linked to the self-association of tubulin heterodimers. The dash dot ($\cdot - \cdot -\cdot$) line represents the fit to the binding constants ($\oplus$) originally reported by Frigon and Timasheff [3,4], and gives a value of 1.065 (± 0.024) Mg^{2+} linked to association. Panels A and B: The various lines represent fits using the binding constants from the $\hat{s}_{20,w}$ fits (panel A) or ΔC fits (panel B) using the $N^{2/3}$ ($\blacksquare$), sphere linear ($\bullet$), 21-bead linear ($\blacktriangle$), helical spheres ($\blacktriangledown$), 21-bead helical ($\blacklozenge$) and a 42-bead helical model ($\blacktriangleleft$), respectively. Panel A: The values from the $N^{2/3}$ model, sphere linear, 21-bead linear model, helical spheres, 21-bead helical and a 42-bead helical model $\hat{s}_{20,w}$ fits are 0.717 (± 0.049), 0.887 (± 0.059), 0.787 (± 0.057), 0.871 (± 0.058), 0.795 (± 0.054) and 0.815 (± 0.055), respectively. Panel B: The values from the $N^{2/3}$ model, sphere linear, 21-bead linear model, helical spheres, 21-bead helical and 42-bead helical model $\hat{s}_{20,w}$ fits are 0.754 (± 0.048), 0.985 (± 0.064), 0.872 (± 0.060), 0.950 (± 0.062), 0.866 (± 0.057) and 0.902 (± 0.060), respectively.

models (1.35–1.73-fold) and the $N^{2/3}$ model (2.11–4.06-fold). Wyman analysis of the data for each assembly model (Fig. 5B) gives an average value of 0.888 ± 0.073 Mg^{2+} ions gained upon assembly. The global K_{iso} values from direct

boundary fitting are generally 20–30% smaller than the weight average estimates at the lower Mg^{2+} concentrations, and 5–10% smaller at the higher Mg^{2+} concentrations. If the fitting is repeated with g fixed at 0.018, the range of differences are significantly reduced (from 10 to 2–3%). The remaining differences appear to reflect the ability of the direct boundary fitting to ignore the larger aggregates when fitting the boundary shape, something not possible with the weight average. This may also reflect relatively less irreversible aggregation at higher Mg^{2+} concentrations (see vinblastine results below).

To further test the application of these models to indefinite self-association reactions, we analyzed vinblastine-induced spiral formation. This analysis requires the use of a ligand mediated model involving K_1, ligand binding, and K_2, indefinite association of liganded protein [9,10] that is altered to include variable $S(N)$ functions. Weight average results are presented in Fig. 8. Both the $N^{2/3}$ and the 21-bead helical models fit the data equally well, although, as expected, the overall K_1K_2 for the bead model is fourfold larger. A 21-bead linear model also fits the data reasonably well, approaching at asymptote at 25–26 S and deviating from the data at high vinblastine concentrations, consistent with the asymptote of the 21-bead $S(N)$ function. This deviation is the first indication of partial discrimination between these models, although still larger $\hat{s}_{20,w}$ values are required for statistically significant deviations. The overall K_1K_2 for the 21-bead linear model is 8.5- and 34-fold larger than for the $N^{2/3}$ and the 21-bead helical models, consistent with the shapes of these $S(N)$ models.

The K_1 K_2 values extracted by this ligand-mediated analysis are related to K_{iso} by the formula [5,6]

$$K_{2,app} = K_2 / \left[1 + \left(1/K_1 [\text{Drug}]_{\text{free}} \right) \right]^2$$

which implies each sample, at a fixed free drug concentration, should be analyzable with ISODESfitter to determine $K_{2,app}$. Thus, to investigate the shape of the vinblastine induced reaction boundaries, data at 1.01 μM vinblastine were analyzed
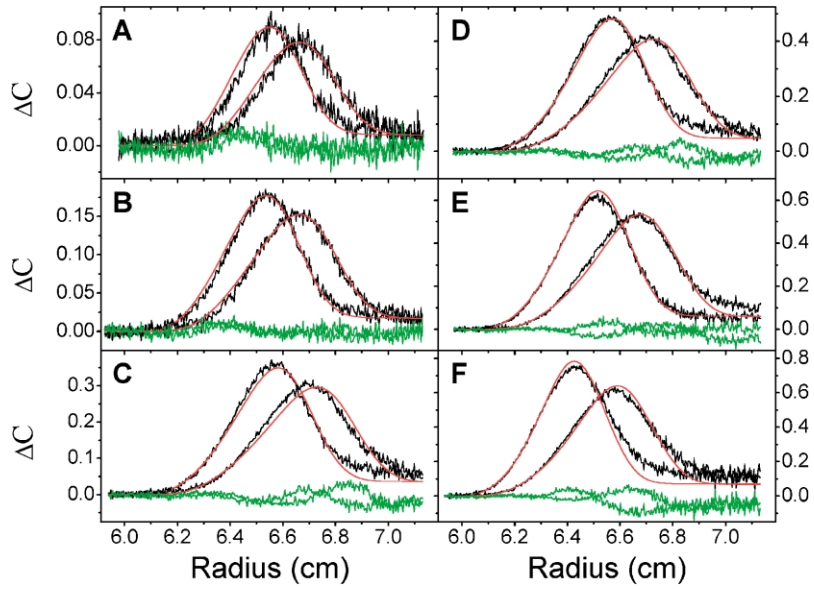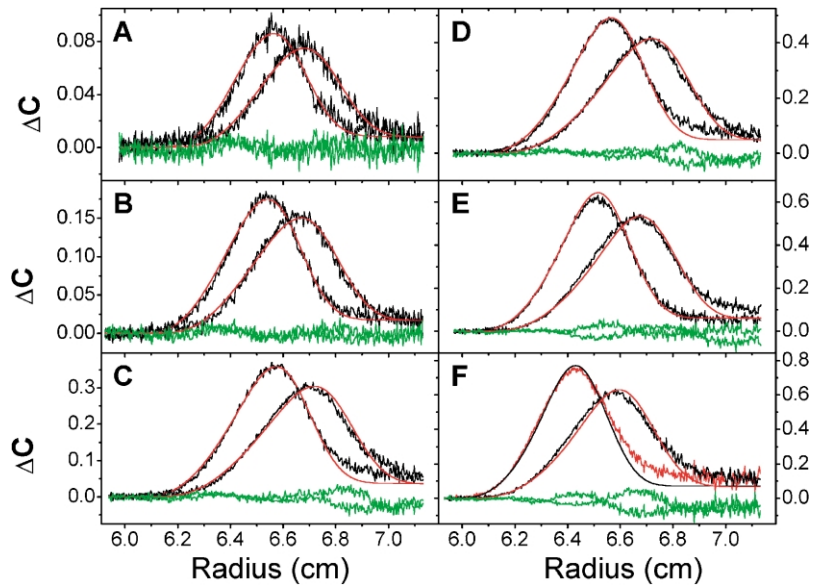
Fig. 6.

Fig. 7.

by ISODESfitter (Fig. 9). At this degree of associ-ation ($\hat{s}_{20,w}$ = 9.60 S) all three models accurately describe the shape of the boundary. This is further evidence that in this instance tubulin is forming a distribution of ligand-induced spirals, a model derived independently from synchrotron scattering data [46]. While the fitting cannot exclude the $N^{2/3}$ model, it does suggest in this instance the absence of aggregation and isotype or nucleotide heterogeneity. Vinca alkaloids are known to protect tubulin by inducing these stable spirals and pre-venting irreversible alternate pathways. Mg^{2+} alone does not appear to prevent aggregation efficiently. Global fitting of these data requires the inclusion of this ligand-mediated model into ISODESfitter. For reasons discussed below this will be presented in a more complete reinvestigation of vinca alkaloid-induced tubulin spiral formation ([9,10,48,49]).

4. Discussion

We have demonstrated the development of a software package ISODESfitter for the analysis of sedimentation velocity patterns for indefinite pol-ymerizing systems. HYDRO was used to develop functional relationships between $S(N)$ vs. N-mer functions and the degree of oligomerization, N, and these functions were incorporated into both weight average and ΔC boundary fitting routines. The results demonstrate that direct fitting to bound-
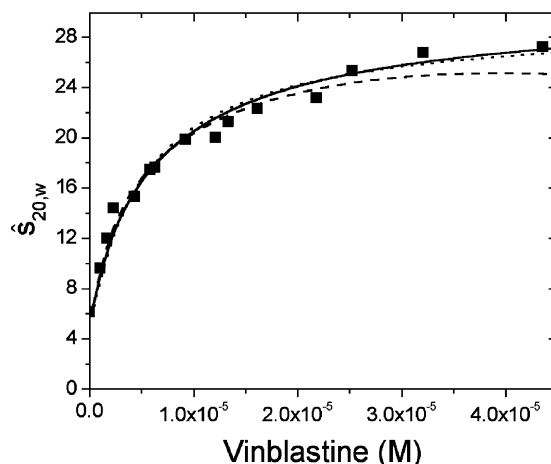

Fig. 8. A comparison of fitting $\hat{s}_{20,w}$ data for vinblastine induced tubulin self-association using different models for polymer formation. The closed symbols (■) represent the $\hat{s}_{20,w}$ values for 2 μM tubulin at 0–40 μM vinblastine in a buffer consisting of 80 mM Pipes, 50 μM GDP, 0.5 mM $MgCl_2$, 0.5 mM EGTA, pH 6.8 at 19.7 °C. The curves represent the fits to the $\hat{s}_{20,w}$ data assuming an $N^{2/3}$ (——), 21-bead linear (– – –), or 21-bead helical (·····) relationship between the sedimentation coefficients and the polymers formed. The K_1K_2 values obtained were 3.82×10^{12} M^{-2} ($1.43\times10^5\times2.67\times10^7$), 1.29×10^{12} M^{-2} ($8.44\times10^3\times1.53\times10^{10}$), and 1.52×10^{13} M^{-2} ($7.98\times10^4\times1.91\times10^8$) for $N^{2/3}$, 21-bead linear, and 21-bead helical fits, respectively.

Fig. 6. A plot of the global fit of the 10 mM Mg^{2+} data by ISODESfitter using the 42-bead helical model. Panels A–F represent the sedimentation velocity experiments performed for 2, 4, 8, 10, 12, and 14 μM tubulin. The sedimentation velocity data is represented by the black curves plotted as ΔC, the difference between pairs of absorbance scans, vs. the radial position. The red curves represent the simulated fits from isodesmic fitter for this data. The green lines represent the residuals of the fits. Eight pairs of scans were used in the fitting but only two pairs are shown for clarity. The deviation pattern in the residuals is observed in all of the Mg^{2+} data sets, and suggests the presence of heterogeneity in K_{iso} and the presence of higher order polymers. A summary of the global ΔC fits to all six models (Fig. 1) is listed in Table 3.

Fig. 7. A plot of the individual fits of the 10 mM Mg^{2+} data by ISODESfitter using a 42-bead helical model. Panels A–F represent the sedimentation velocity experiments performed for 2, 4, 8, 10, 12, and 14 μM tubulin with corresponding K_{iso} values of 2.79×10^5, 2.43×10^5, 2.12×10^5, 2.17×10^5, 2.29×10^5, and 2.44×10^5 M^{-1}. The sedimentation velocity data is represented by the black curves plotted as ΔC, the difference between pairs of absorbance scans, vs. the radial position. The red curves represent the simulated fits from isodesmic fitter for this data. The green lines represent the residuals of the fits. Eight pairs of scans were used in the fitting but only two pairs are shown for clarity. The deviation pattern in the residuals has changed and now one can see the presence of heterogeneity in K_{iso} by the range of best fitted values, $2.17–2.79\times10^5$ M^{-1}. The presence of higher order polymers in the 8, 10 and 14 M tubulin samples is evident at the base of those cells.

Table 3
Summary of ΔC fitting of sedimentation velocity data

		$[Mg^{2+}]$ (mM)					
		0	0.5	1	2	5	10
$N^{2/3}$	RMS$_{[fit]}$ (O.D.)	0.0213	0.0173	0.0182	0.0244	0.0265	0.0229
	K_{iso} (M^{-1})	6.36×10^3	8.90×10^3	1.22×10^4	2.68×10^4	4.58×10^4	8.09×10^4
	$\Delta G° K_{iso}$ (kcal mol^{-1})	−4.82	−5.00	−5.18	−5.61	−5.90	−6.22
Linear (spheres)	RMS$_{[fit]}$ (O.D.)	0.0212	0.0177	0.0168	0.0199	0.0184	0.0341
	K_{iso} (M^{-1})	1.22×10^4	1.79×10^4	2.54×10^4	6.75×10^4	1.46×10^5	3.15×10^5
	$\Delta G° K_{iso}$ (kcal mol^{-1})	−5.18	−5.39	−5.58	−6.12	−6.54	−6.96
Linear (21 beads)	RMS$_{[fit]}$ (O.D.)	0.0213	0.0183	0.0174	0.0217	0.0208	0.0218
	K_{iso} (M^{-1})	8.35×10^3	1.20×10^4	1.67×10^4	3.98×10^4	7.33×10^4	1.58×10^5
	$\Delta G° K_{iso}$ (kcal mol^{-1})	−4.97	−5.17	−5.35	−5.83	−6.16	−6.58
Helical (spheres)	RMS$_{[fit]}$ (O.D.)	0.0213	0.0176	0.0167	0.0200	0.0184	0.0324
	K_{iso} (M^{-1})	1.46×10^4	2.16×10^4	3.06×10^4	8.07×10^4	1.68×10^5	3.42×10^5
	$\Delta G° K_{iso}$ (kcal mol^{-1})	−5.27	−5.49	−5.68	−6.21	−6.62	−7.01
Helical (21 beads)	RMS$_{[fit]}$ (O.D.)	0.0213	0.0181	0.0173	0.0214	0.0199	0.0212
	K_{iso} (M^{-1})	9.84×10^3	1.42×10^4	1.97×10^4	4.74×10^4	8.89×10^4	1.80×10^5
	$\Delta G° K_{iso}$ (kcal mol^{-1})	−5.06	−5.26	−5.44	−5.92	−6.27	−6.66
Helical (42 beads)	RMS$_{[fit]}$ (O.D.)	0.0213	0.0179	0.0171	0.0208	0.0190	0.0222
	K_{iso} (M^{-1})	1.15×10^4	1.67×10^4	2.33×10^4	5.75×10^4	1.16×10^5	2.31×10^5
	$\Delta G° K_{iso}$ (kcal mol^{-1})	−5.14	−5.35	−5.53	−6.03	−6.41	−6.79

These sedimentation velocity experiments were performed at 4 °C, $\lambda = 278$ nm, and 42 000 rpm using the 25 mM Pipes buffer at pH 6.8 with 50 μM GDP and 50 mM KCl. The global fits with ISODESfitter each used a fixed sedimentation coefficient value for tubulin, corresponding to the appropriate Mg^{2+} buffer and $g=0$ for all fits.

ary shape is a valid approach and has several advantages over weight average analysis including the ability to do both global fits of all experiments and individual fits of each experiment. For the Mg^{+2}-dependent self-association analysis, the corresponding ΔG values from $\hat{s}_{20,w}$ analysis were on average -0.14 ± 0.06 kcal mol^{-1} more favorable (20–30% large K_{iso}) than those from ΔC curve fitting for low divalent concentrations. (On average half of this can be accounted for by using $g = 0.018$ for hydrodynamic nonideality. Since, there is no consistent improvement in the RMS of the ΔC fits these results are not reported here.) The ΔC curve fitting method ignores large inactive material resulting in noticeable non-random residuals for the fits near the base of the cells. These residuals, therefore, indicate the presence of larger species not present in the model for association, which in this case represent irreversibly aggregated

tubulin. This indicates that the ΔC curve fitting procedure is a more accurate and robust method for analyzing associating systems since it selects the reversible components in the boundary. $\hat{s}_{20,w}$ analysis also provides reasonably accurate values for the binding constants involved, especially in the absence of irreversible heterogeneity. Since $\hat{s}_{20,w}$ analysis can be achieved more rapidly, it should preferentially be the initial method used to analyze associating systems. The ΔC curve fitting method should complement the $\hat{s}_{20,w}$ analysis, potentially leading to the identification of aggregation and more accurate estimates of K_{iso}.

The heterogeneity observed in the 10 mM Mg^{+2} data (Fig. 6) suggests a combination of heterogeneity in reaction energetics, K_{iso}, and the presence of larger irreversible aggregates. In this case the binding constants do not systematically decrease with increasing concentration, a diagnos-
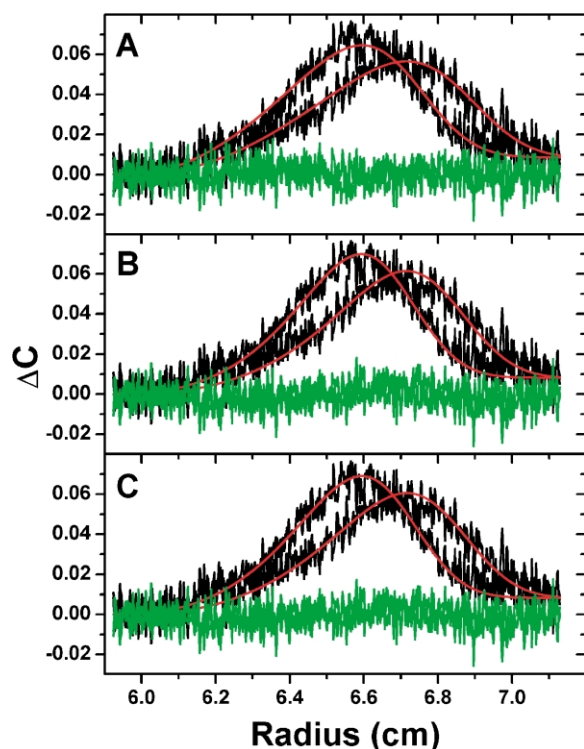
Fig. 9. A comparison of ISODES fitting of ΔC data from vinblastine induced tubulin self-association sedimentation velocity data. Tubulin at a concentration of 2 μM was spun with 1.01 μM vinblastine in an 80 mM Pipes, 50 μM GDP, 0.5 mM MgCl$_2$, pH 6.8 buffer at 19.7 °C. Three different models were used in ISODES: $N^{2/3}$ (panel A), 21-bead linear (panel B), or 21-bead helical (panel C) relationship between the sedimentation coefficients and the polymers formed. The sedimentation velocity data is represented by the black curves plotted as ΔC vs. the radial position. The red curves represent the simulated fits from isodesmic fitter for these data using the appropriate model for association. Finally the green lines represent the residuals of the fits. Eight pairs of scans were used in the fitting but only two pairs are shown for clarity. These fits described the data quite well and verify the helical model, although at this low extent of association we cannot distinguish between the three models. The K_{iso} values obtained were 7.46×10^5, 1.78×10^6, and 1.93×10^6 for $N^{2/3}$, 21-bead linear, and 21-bead helical fits, respectively, with corresponding RMS values of 0.0589, 0.0609 and 0.0596.

tic of the presence of irreversible aggregates [56]. This would apply in the extreme to a fixed percentage of aggregates in each solution, as if the stock solution were contaminated. Alternatively, aggregates can form during sample preparation,

and thus vary from sample to sample, typically being worse at lower protein concentrations. Sample to sample variation appears to be what we observe for many of these experiments, especially the 5 mM Mg^{+2} data. Alternate models or complexities to the model include tubulin isotype heterogeneity [9] causing heterogeneity in K_{iso}, nucleotide content heterogeneity also causing heterogeneity in K_{iso}, or Mg^{2+}-induced rings contributing significantly to the boundary shapes. Significant ring formation is highly unlikely at low Mg^{2+} concentrations, although it may very well contribute to the more significant deviations observed by weight average analysis at the higher Mg^{2+} concentrations. The method of sample preparation should convert all GTP-tubulin to GDP-tubulin. To further test this samples were also prepared by a double spun column method (9, 36) that produces only GDP-tubulin. The same fitting deviations were observed for these samples (data not shown) and thus GTP/GDP nucleotide heterogeneity is ruled out as a cause. Isotype heterogeneity cannot be excluded, but previous studies with vinblastine induced spiral formation revealed the absence of isotype heterogeneity [9]. At the very least, isotype heterogeneity should not give rise to variable binding constants, but should generate a superposition of polymers with mixed association behavior. The goodness of fit at the low protein concentrations suggests there is no significant spreading, expected if each isotype associated selectively. We conclude the measured values of K_{iso} are average values for these mixed polymers and, in fact, reflect typical experimental uncertainty for this type of analysis. For example, at 10 mM Mg^{2+}, the average standard deviation about the mean value of K_{iso} (for the six data sets fit individual with the six models) is 12.7%.

These results suggest the new HYDRO derived models do not improve the goodness of fit for either the Mg^{+2} dependent or the vinblastine dependent reactions. Thus, fitting velocity data alone with these various models will not allow one to discriminate between them and thus choose the best quaternary model (Fig. 1) to describe the data. Apparently, the indefinite model involves so many species that compensation in K_{iso} can make any specific indefinite sedimentation distribution

look like any other within experimental error, at least up to the asymptotic limit of maximum S_N. Independent information from cryo-EM or synchrotron scattering must provide the appropriate model. However, the energetics of association according to that model are more accurately measured by using the correct HYDRO derived model for indefinite boundary shape analysis. This does not appear to apply to difference comparisons, like those in a Wyman plot, where the effects of solution conditions are correctly inferred, since the slopes were relatively constant regardless of the model used to fit the data. Thus, $\Delta\Delta G$ analysis may be unaffected as well. This will be tested in a reanalysis of tubulin spiral potential induced by various vinca alkaloids [9,10].

There are still a number of limitations to this approach that need improvement. The first is a limitation of HYDRO. To build a 50-mer using a 42-bead model requires 2100 beads. The current version of HYDRO is limited to 2000 beads. The number of beads can be increased in the code but significant increases are limited by the available computer memory. Going to 5000 beads required over 900 MB of RAM, i.e. memory usage increases as $(\#\text{beads})^3$. If one wished to construct models derived from pdb files this is also possible using available software [50]. For example, the cyro-EM structure of the tubulin dimer, tub1.pdb, was converted to a bead model involving 867 beads. The use of this model in polymer building offers more severe restraints on array sizes and memory usage. An alternative is to construct shell models, thus reducing the number of beads to that required for defining the outmost surface of the molecule. Given the inability to resolve the best indefinite model by direct boundary fitting, a shell model may not be an improvement.

A second limitation is with the finite element solution to the Lamm equation for reversibly indefinite associating macromolecules. At the base of the cell protein concentration builds up rapidly and thus polymerization is driven toward larger and larger polymer sizes. Above K_{iso} values of 5×10^6 M^{-1}, this routine consistently fails while making calculations at the high concentrations at the base of the cell. Increasing the point density, and reducing the time between simulations to 0.01

s helps, but does not consistently solve the problem. Failure of the finite element solution will be a problem for all cases where large polymers are part of the mechanism. Additional solutions to this limitation are being explored. One additional caveat to the use of global boundary methods is that a global fit to six channels of data, floating K_{iso} and all the local concentrations through 250–500 iterations, can take 6–12 h of computer time on a 1.7 GHz Pentium 4 processor with 512 MB of RAM. Pre-analysis by fitting weight average data is strongly recommended to limit choice of models and parameter estimates.

This curve fitting approach may also require certain theoretical extensions to the models. (1) Many of the prior systems described as isodesmic actually revealed a K_2 value that was distinct from the K_{iso} value [26]. (2) The development of a ligand-mediated model fitter appropriate to global analysis of vinca alkaloid-induced self-association of tubulin is in progress. (3) The general isodesmic model has previously been modified to yield an isoenthalpic model consisting of a constant enthalpy of association and a polymer-size-dependent entropy [51]. The isoenthalpic model reflects the fact that each tubulin heterodimer loses translational and rotational entropy upon association, but the growing polymer has already lost some fraction of this entropy, and thus dimer addition to larger polymers causes a more substantial loss of freedom for the dimer. Since loss of translational and rotational entropy opposes association, K_{iso} should decrease with polymer length. This decrease over the first association step, K_2, should at least be in the range of half of the typical value for loss of translational and rotational entropy, 20.7 eu, estimated for rigid body association [52]. Incorporation of these alternate models into ISODESfitter and Sedanal [55] as fitting options is currently in development.

5. Conclusions

A software package ISODESfitter has been developed and tested for the analysis of sedimentation velocity boundary shapes of indefinite polymerizing macromolecular systems. Experiments may be analyzed individually or globally, and procedures

for developing models for the sedimentation coefficients of the oligomers and diagnosis of heterogeneity in K_{iso} as well as irreversible aggregation are described. The ISODES or ΔC curve fitting approach is useful in conjunction with weight average analysis, and offers more robust and accurate estimation of equilibrium constants for indefinite polymerizing systems.

Acknowledgments

References

[1] T. Svedberg, R. Fähraeus, A new method for the determination of the molecular weight of the proteins, J. Am. Chem. Soc. 48 (1926) 430–438.

[2] J.J. Correia, Analysis of weight average sedimentation velocity data, Methods Enzymol. 321 (2000) 81–100.

[3] R.P. Frigon, S.N. Timasheff, Magnesium-induced self-association of calf brain tubulin. I. Stoichiometry, Biochemistry 14 (1975) 4559–4566.

[4] R.P. Frigon, S.N. Timasheff, Magnesium-induced self-association of calf brain tubulin. II. Thermodynamics, Biochemistry 14 (1975) 4567–4573.

[5] G.C. Na, S.N. Timasheff, Velocity sedimentation study of ligand-induced protein self-association, Methods Enzymol. 117 (1985) 459–495.

[6] G.C. Na, S.N. Timasheff, Measurement and analysis of ligand-binding isotherms linked to protein self-associations, Methods Enzymol. 117 (1985) 496–519.

[7] G.C. Na, S.N. Timasheff, Interaction of vinblastine with calf brain tubulin: multiple equilibria, Biochemistry 25 (1986) 6214–6222.

[8] G.C. Na, S.N. Timasheff, Interaction of vinblastine with calf brain tubulin: effects of magnesium ions, Biochemistry 25 (1986) 6222–6228.

[9] S. Lobert, A. Frankfurter, J.J. Correia, Binding of vinblastine to phosphocellulose-purified and alpha beta-class III tubulin: the role of nucleotides and beta-tubulin isotypes, Biochemistry 34 (1995) 8050–8060.

[10] S. Lobert, J.J. Correia, Energetics of vinca alkaloid interactions with tubulin, Methods Enzymol. 323 (2000) 77–103.

[11] J.C. Lee, N. Tweedy, S.N. Timasheff, In vitro reconstituion of calf brain microtubules: effects of macromolecules, Biochemistry 17 (1978) 2783–2790.

[12] P.A. Curmi, S.S.L. Anderson, S. Lachkar, et al., The stathmin/tubulin interaction in vitro, Biol. Chem. 272 (1997) 25029–25036.

[13] L. Jourdain, P. Curmi, A. Sobel, D. Panataloni, M.F. Carlier, Stathmin: a tubulin-sequestering protein which forms a ternary T2S complex with two tubulin molecules, Biochemistry 36 (1997) 10817–10821.

[14] J. Behlke, O. Ristau, Molecular mass determination by sedimentation velocity experiments and direct fitting of the concentration profiles, Biophys. J. 72 (1997) 428–434.

[15] J.S. Philo, An improved function for fitting sedimentation velocity data for low-molecular-weight solutes, Biophys. J. 72 (1997) 435–444.

[16] J.S. Philo, A method for directly fitting the time derivative of sedimentation velocity data and an alternative algorithm for calculating sedimentation coefficient distribution functions, Anal. Biochem. 179 (2000) 151–163.

[17] P. Schuck, Sedimentation analysis of noninteracting and self-associating solutes using numerical solutions to the Lamm equation, Biophys. J. 75 (1998) 1503–1512.

[18] P. Schuck, B. Demeler, Direct sedimentation analysis of interference optical data in analytical ultracentrifugation, Biophys. J. 76 (1999) 2288–2296.

[19] P. Schuck, Sedimentation equilibrium analysis of interference optical data by systematic noise decomposition, Anal. Biochem. 272 (1999) 199–208.

[20] P. Schuck, M.A. Perugini, N.R. Gonzales, G.J. Howlett, D. Schubert, Size-distribution analysis of proteins by analytical ultracentrifugation: strategies and application to model systems, Biophys. J. 82 (2002) 1096–1111.

[21] W.F. Stafford III, Modern analytical ultracentrifugation: acquisition and interpretation of data for biological and synthetic polymer systems, in: T.M. Schuster, T.M. Laue (Eds.), Sedimentation Boundary Analysis of Interacting Systems: Use of the Apparent Sedimentation Coefficient Distribution Function, Birkhäuser, Boston, 1994, p. 119.

[22] W.F. Stafford III, Boundary analysis in sedimentation transport experiments: a procedure for obtaining sedimentation coefficient distributions using the time derivative of the concentration profile, Anal. Biochem. 203 (1992) 295–301.

[23] R.R. Holloway, D.J. Cox, Computer simulation of sedimentation in the ultracentrifuge. VII. Solutes Undergoing Indefinite Self-Association, Arch. Biochem. Biophys. 160 (1974) 595–602.

[24] W.F. Stafford, Time difference sedimentation velocity analysis of rapidly reversible interacting systems: determination of equilibrium constants by global non-linear curve fitting procedures, Biophys. J. 74 (1998) A301.

[25] P.D. Jeffrey, B.K. Milthorpe, L.W. Nichol, Polymerization pattern of insulin at pH 7.0, Biochemistry 15 (1976) 4660–4665.

[26] A. Henniker, G.B. Ralston, Reinvestigation of the thermodynamics of spectrin self-association, Biophys. Chem. 52 (1994) 251–258.

[27] R. Josephs, H. Eisenberg, E. Reisler, in: R. Jaenicke, E. Helmreich (Eds.), Protein–Protein Interactions, Springer, New York, 1972, p. 57.

[28] R. Smith, Self-association of myelin basic protein: enhancement by detergents and lipids, Biochemistry 21 (1982) 2697–2701.

[29] G. Rivas, A. Lopez, J. Mingorancei, et al., Magnesium-induced linear self-association of the FtsZ bacterial cell division protein monomer: the primary steps for FtsZ assembly, J. Biol. Chem. 275 (2000) 11740–11749.

[30] G. Rivas, J.A. Fernandez, A.P. Minton, Direct observation of the enhancement of noncooperative protein self-assembly by macromolecular crowding: indefinite linear self-association of bacterial cell division protein FtsZ, Proc. Natl. Acad. Sci. 98 (2001) 3150–3155.

[31] J.L. Cole, J.D. Gehman, J.A. Shafer, L.C. Kuo, Solution oligomerization of the rev protein of HIV-1: implications for function, Biochemistry 32 (1993) 11769–11775.

[32] J.M. Claverie, H. Dreux, R. Cohen, Sedimentation of generalized systems of interacting particles. I. Solution of systems of complete Lamm equations, Biopolymers 14 (1975) 1685–1700.

[33] G.P. Todd, R.H. Haschemeyer, General solution to the inverse problem of the differential equation of the ultracentrifuge, Proc. Natl. Acad. Sci. 78 (1981) 6739–6743.

[34] J.A. Nelder, R. Mead, A simplex method for function minimization, Comput. J. 7 (1965) 308–313.

[35] J.G. de la Torre, S. Navarro, M.C. Lopez Martinez, F.G. Diaz, J.J. Lopez Cascales, HYDRO: a computer program for the prediction of hydrodynamic properties of macromolecules, Biophys. J. 67 (1994) 530–531.

[36] R.C. Williams, J.C. Lee, Preparation of tubulin from brain, Methods Enzymol. 85 (1982) 376–385.

[37] J.J. Correia, L.T. Baty, R.C. Willaims Jr., Mg^{2+} dependence of guanine nucleotide binding to tubulin, J. Biol. Chem. 262 (1987) 17278–17284.

[38] H.W. Detrich III, R.C. Williams Jr., Reversible dissociation of the alpha beta dimer of tubulin from bovine brain, Biochemistry 17 (1978) 3900–3907.

[39] S. Liu, W.F. Stafford III, An optical thermometer for direct measurement of cell temperature in the Beckman instruments XL-A analytical ultracentrifuge, Anal. Biochem. 224 (1995) 199–202.

[40] H.S. Penefsky, Reversible binding of Pi by beef heart mitochondrial adenosine triphosphatase, J. Biol. Chem. 252 (1977) 2891–2899.

[41] J.J. Correia, B.M. Chacko, S. Lam, K. Lin, Sedimentation studies reveal a direct role of phosphorylation in Smad3:Smad4 homo- and hetero-trimerization, Biochemistry 40 (2001) 1473–1482.

[42] J.J. Correia, S.P. Gilbert, M.L. Moyer, K.A. Johnson, Sedimentation studies on the kinesin motor domain constructs K401, K366, and K341, Biochemistry 34 (1995) 4898–4907.

[43] J.C. Lee, R.P. Frigon, S.N. Timasheff, The chemical characterization of calf brain microtubule protein subunits, J. Biol. Chem. 248 (1973) 7253–7262.

[44] J.C. Lee, S.N. Timasheff, Partial specific volumes and interactions with solvent components of proteins in guanidine hydrochloride, Biochemistry 13 (1974) 257–265.

[45] J.G. de la Torre, J.M. Andreu, Hydrodynamic analysis of tubulin dimer and double rings, J. Mol. Biol. 238 (1994) 223–225.

[46] J.F. Diaz, E. Pantos, J. Bordas, J.M. Andreu, Solution structure of GDP-tubulin double rings to 3 nm resolution and comparison with microtubules, J. Mol. Biol. 238 (1994) 214–225.

[47] J.L. Hodgkinson, T. Hutton, F.J. Medrano, J. Bordas, X-ray solution scattering studies on vinblastine-induced polymers of microtubule protein: structural characterisation and effects of temperature, J. Struct. Biol. 109 (1992) 28–38.

[48] S. Lobert, A. Boyd, J.J. Correia, Divalent cation and ionic strength effects on vinca alkaloid-induced tubulin self-association, Biophys. J. 72 (1997) 416–427.

[49] S. Lobert, B. Vulevic, J.J. Correia, Interaction of vinca alkaloids with tubulin: a comparison of vinblastine, vincristine, and vinorelbine, Biochemistry 35 (1996) 6806–6814.

[50] J.G. de la Torre, M.L. Huertas, B. Carrasco, Calculation of hydrodynamic properties of globular proteins from their atomic-level structure, Biophys. J. 78 (2000) 719–730.

[51] R.C. Chatelier, Indefinite isoenthalpic self-association of solute molecules, Biophys. Chem. 28 (1987) 121–128.

[52] T. Horton, M. Lewis, Calculation of the free energy of association for protein complexes, Protein Sci. 1 (1992) 169–181.

[53] K.E. van Holde, Physical Biochemistry, second ed., Prentice-Hall, Englewood Cliffs, 1985.

[54] R. Surendran, P. Herman, Z. Cheng, T.J. Daly, J.C. Lee, HIV Rev self-assembly is linked to a molten-globule to compact structural transition, Biophys. Chem. 108 (2004) 101–119.

[55] W.F. Stafford, P.J. Sherwood, Analysis of heterologous interacting systems by sedimentation velocity: curve fitting algorithms for estimation of sedimentation coefficients, equilibrium and kinetic constants, Biophys. Chem. 108 (2004) 231–243.

[56] Y. Xu, Characterization of macromolecular heterogeneity by equilibrium sedimentation techniques, Biophys. Chem. 108 (2004) 141–163.